ORIGINAL RESEARCH

Influence of tailored CuO and Al/CuO nanothermites on the thermocatalytic degradation of nitrocellulose and combustion performance of AP/HTPB composite propellant

Ningning Zhao · Haixia Ma · Ergang Yao · Zhong Yu · Ting An ·
Fengqi Zhao · Xiaojiao Yu

Abstract Al/CuO nanothermites have displayed unique catalytic activities in accelerating the thermolysis of nitrocellulose (NC) and combustion characteristics of AP/HTPB propellant depending on the morphology of CuO. The kinetic triplet of NC-based composites was determined by multi- isoconversional methods, whereas the reaction models were reconstructed by employing a modified Šesták–Berggren equation based on the combined kinetic analysis. DSC and TG-FTIR results revealed that CuO and Al/CuO play crucial roles in accelerating the dissociation of –O–NO$_2$ bond and the coacervate phase to change the pyrolysis mechanism of NC from an autocatalytic reaction to a modified *n*-th order reaction model. It was also demonstrated that nanothermites were provided with a low starting temperature of pyrolysis, reduced exothermic peak temperature, low activation energy, and high total weight loss, confirming their better catalytic activity than their corresponding CuO, of which Al/CuO nanothermite, containing the gypsophila paniculata-like CuO, performs the best. Further, the shape of CuO was found to be significant in enhancing the burning rate of AP/HTPB propellant containing thermites, with the gypsophila paniculata-like presenting the best catalytic effect (43% improvement). Hence, introducing well-defined nanostructures is a promising way to improve the pyrolysis and combustion of energetic materials.

N. Zhao (✉) · Z. Yu · X. Yu
School of Science, Xi'an University of Technology,
Xi'an 710054, Shaanxi, China
e-mail: zhaonn@xaut.edu.cn

H. Ma (✉)
School of Chemical Engineering, Northwest University,
Xi'an 710069, Shaanxi, China
e-mail: mahx@nwu.edu.cn

E. Yao · T. An · F. Zhao
Science and Technology On Combustion and Explosion
Laboratory, Xi'an Modern Chemistry Research Institute,
Xi'an 710065, Shaanxwi, China

Introduction

Homogeneous and heterogeneous solid propellants usually contain various components such as oxidizer, fuel, adhesive, modifier or catalyst, plasticizer, curing agent, stabilizer, and other additives (crosslinker, opacifier, desensitizing agent, etc.). Among them, the oxidizer is the principal component, which could rapidly release mass energy via burning. Cellulosic based energetic polymers such as nitrocellulose (NC), are typical oxidizers in military and civilian applications, which can also serve the basis to develop new

energetic materials, such as propellants and explosives (Tarchoun et al. 2020a, b, c, 2021a, b, c). NC is commonly employed in smokeless powders (Chajistamatiou et al. 2016; Botelho et al. 2015), guns (Damse et al. 2009; Shen et al. 2019), blasting gelatin, dynamites, and single- (Jain et al. 2016), double- (Krumlinde et al. 2016; Boulkadid et al. 2019) and triple-base homogeneous propellants (Mendonça-Filho et al. 2019; Liang et al. 2018), in addition to other civilian applications (Yang et al. 2017) due to its high flammability and explosiveness without residual char (Yoon et al. 2016). The thermodynamic properties of oxidizers could appropriately demonstrate the burning performances of the relevant propellants based on them (Singh et al. 2009; Yan et al. 2016). Researchers have shown that the modifiers or catalysts could significantly influence the burning rate and pressure exponents of solid propellants due to their catalytic capacity for the thermal degradation of oxidizers. Therefore, the catalytic effect of catalysts including transition metal oxides (TMOs) and metastable intermolecular composites (MICs) (Mei et al. 2019), on the thermal decomposition process of oxidants has become a research focus (Chaturvedi et al. 2019; Dai et al. 2018).

As representatives of semiconductor materials and catalysts, TMOs can supply abundant electron transfer orbits during redox reactions, thus promoting electron transfer on top of oxidizers (Hu et al. 2020) and changing their decomposition routes and mechanisms. Nanothermites are typical MICs, which contain aluminum (Al) and one or several TMOs that result in enhancing the reaction activity (Stiegman et al. 2009). Based on previous reports, catalysts such as Fe_2O_3 (Pourmortazavi et al. 2019; Benhammada et al. 2020a), Cr_2O_3 (Guo et al. 2019), NiO (Wei et al. 2009), and nanothermites Al/Fe_2O_3 (Pourmortazavi et al. 2014; Li et al. 2013) and Al/CuO (Kim et al. 2019a; Saceleanu et al. 2018) have tremendous potential superiority in the thermal performances and pyrolysis mechanisms of NC. The nonisothermal decomposition kinetics and isoconversional kinetic models of NC with and without catalysts are employed to investigate the corresponding thermal decomposition reactions in the literature. It has been observed that the addition of some catalysts, such as α-Fe_2O_3, Al/Fe_2O_3, and Cr_2O_3, could remarkably decrease the values of apparent activation energy, peak temperature, and the critical temperature for the thermal

explosion of NC-based composites. The pyrolysis behaviors of energetic materials could be evaluated more exactly and detailedly by employing thermogravimetry coupled with Fourier transform infrared spectroscopy (TG-FTIR) (Benhammada and Tracheet 2020). Based on the high specificity and sensitivity of TG-FTIR hyphenated techniques, the rupture of O–NO_2 bond and secondary self-catalyzed reactions that occur in the coacervate phase are promoted during the decomposition process. Further, the evolved gaseous products during the pyrolysis of NC-based composites are diverse due to the catalytic effect of nano-sized additives compared with that of the pristine NC.

TMOs and MICs are used as active ingredients in solid propellants, which have been displayed to significantly improve the ignition and combustion performances of propellants (Ru et al. 2016; Pang et al. 2019). Double-base propellants including nanothermites Al/PbO, Al/CuO and Al/Bi_2O_3 have been proven to increase the energy release rate of propellants, yet their effects on pressure exponent are not obvious (An et al. 2011). Fe_2O_3 particles and the corresponding Al/Fe_2O_3 nanothermites increase the combustion rate to varying degrees and reduce the pressure index of AP/HTPB composite propellant systems contributing to the structural effect of nano Fe_2O_3 with various sizes and morphologies (Zhao et al. 2014). Compared with blank propellants, the burning rate of AP-CMDB propellant (Hao et al. 2019) has risen by 22.2% with the presence of CuO nanoparticles (NPs). Ultrahigh-burning rate propellants including nano TiO_2, and fluorescing propellants including quantum dots (QDs) (Thomas et al. 2018), have been developed to increase the aging stability of propellant formulations by introducing QDs or nano TiO_2.

With the deepening of research, more TMOs and MICs are being developed and have tremendous potential superiority in thermal catalytic activity for oxidants, and combustion catalytic performance for solid propellants. In a previous study, we demonstrated the remarkable role of the different morphologies of CuO and corresponding nanothermites on NC decomposition based on nonisothermal decomposition kinetics (Yao et al. 2020). In this study, two novel CuO NPs—gypsophila paniculata- and crab cactus-like NPs—with specific surface areas of 90.14 and 48.93 m^2/g were prepared by hydrothermal approach and could significantly improve the thermolysis process of

pristine NC. The TG-FTIR hyphenated technique was employed in detecting the free radical or degradation products and deducing the possible catalytic mechanism of catalysts. Depending on the multi isoconversional analysis, the kinetic triplet activation energy (E_α), pre-exponential factor (A), and reaction model of CuO-NC and Al/CuO-NC complexes were obtained through Kissinger–Akahira–Sunose (KAS), Flynn–Wall–Ozawa (FWO), and Friedman methods (Kim et al. 2019b). The reaction models were reconstructed by introducing a modified Šesták–Berggren empirical equation according to the combined kinetic analysis. Moreover, the prepared CuO and Al/CuO nanothermites were applied to AP/HTPB composite propellants to investigate their application in combustion performances.

Experimental

Synthesis of CuO particles

Compared with our previous work (Yao et al. 2020), two novel types of CuO structures, gypsophila paniculata- and crab cactus-like, marked by CuO(G) and CuO(C),were successfully obtained by the hydrothermal methods. Typically, 0.68 g of copric chloride dihydrate (CuCl$_2$·2H$_2$O, 99.99%, Aladdin Biotechnology Co., Ltd., China) and 0.05 g of sodium dihydngen phoshate anhydrous (NaH$_2$PO$_4$, $\geq$ 99.0%, Aladdin Biotechnology Co., Ltd., China) were added to 20 mL of deionized water with stirring for 30 min to evenly mix the solution. Blue precipitates were obtained by adding 10 mL of sodium hydroxide (NaOH, $\geq$ 98.0%, Aladdin Biotechnology Co., Ltd., China) solution. The resulting suspension were transferred into a Teflon-lined stainless steel autoclave and then carried out at 120 °C for 2 h. After completing the reaction, the precipitate was washed by deionized water and absolute ethyl alcohol (C$_2$H$_5$OH, $\geq$ 98.0%, Aladdin Biotechnology Co., Ltd., China) alternately, and then put them into an oven at 60 °C for 10 h. The obtained dried product was CuO(G). Sample CuO(C) was prepared following the above experimental procedure but adjusting the reaction temperature of 80 °C.

Preparation of Al/CuO thermites

Al/CuO thermites were prepared by the sonication dispersion method in N$_2$ atmosphere using n-hexane as effective dispersants. Firstly, CuO particles and Al nanopowders ($\approx$ 50 nm in average diameter, Jiaozuo Banlv Nano Material Engineering Co., Ltd., China) were dispersed respectively. Secondly, the CuO dispersion and Al dispersion were ultrasonically mixed in the same vessel and processed at 50 °C for 2 h with ultrasound until n-hexane volatilized completely. Finally, the composite materials were obtained by drying under 60 °C for 8 h in the oven.
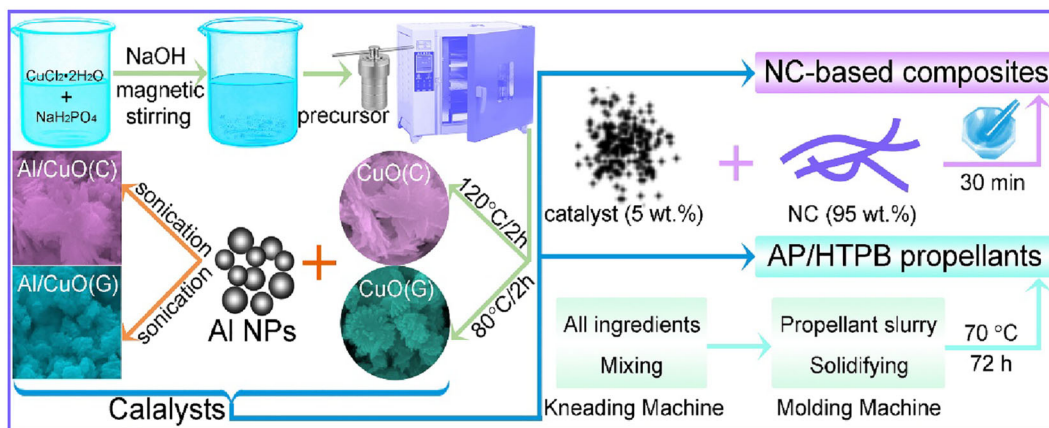
Preparation of NC-based composites

Physical mixtures of CuO particles or Al/CuO thermites—as the catalysts—and NC (nitrogen content of 12.6%, Xi'an Modern Chemistry Research Institute, China) were prepared in an agate mortar with a mass ratio of 1:19 at room temperature. The grinding process was maintained for 30 min to obtain the composite materials, including CuO(C)-NC, Al/CuO(C)-NC, CuO(G)-NC and Al/CuO(G)-NC.

Preparation of propellant formulations

A preliminary AP/HTPB composite propellant—as the blank control group—was composed of 14.3 wt% HTPB, 15.3 wt.% Al powders, 18.4 wt% coarse AP, and 52.0 wt% superfine AP. CuO(C), CuO(G), Al/CuO(C), and Al/CuO(G) were added as catalysts into AP/HTPB composite propellant formulations and marked as C1, C2, T1, and T2, respectively. For the experience groups containing CuO particles—C1 and C2—the contents of other ingredients were the same, except the content of CuO, which was 2.0 wt%. For the experience groups containing thermites—T1 and T2—the contents of other ingredients were the same as those of the blank control group, except the contents of Al powders and thermite were 14.5 and 2.8 wt% respectively. AP/HTPB propellants were obtained following the steps (Zhao et al. 2014): all ingredients were completely mixed in a kneading machine to obtain the propellant slurry; afterward, the slurry was poured into a mold under vacuum conditions and solidified at 70 °C for 72 h.

The above fabricating procedures can be clearly illustrated in Scheme 1

Scheme 1 Schematic diagrams showing preparation procedures of catalysts, NC-based composites and AP/HTPB propellants

Characterization

X-ray diffraction studies on the crystal structure and purity of as-prepared materials were obtained on D/MAX-3C (Rigaku, Japan) device using Cu Kα_1 radiation within $10°–80°$. Composition analysis of materials were studied by EDS (INCAIE350, UK). Grain sizes and microstructures of the as-prepared materials were characterized by using SEM (Quanta 400, USA and TESCAN, Czech Republic) and TEM with high-resolution TEM (Carl Zeiss SMT Pte Ltd., Germany). Thermal behavior were analyzed by DSC (Q2000, TA Co.), furthermore, the kinetic triplet were dealt with the mathematic means based on the DSC data. Gases products from the whole pyrolysis process were detected by TG-FTIR technique at Ar atmosphere. The S_{BET} and pore volume were performed on a JW-BK122W static nitrogen adsorption (Beijing JingweiGaobo, China).

Results and discussion

Characterization of CuO and Al/CuO

The crystalline structure and composition of the as-prepared samples were investigated by XRD technology (Fig. 1). The identifiable and broad diffraction peaks centered at about 32.8°, 35.9°, 39.0°, 49.1°, 54.0°, 58.6°, 61.7°, 66.3°, 68.4°, 72.6°, and 75.5° corresponded to the characteristic (110), (11–1), (111), (20–2), (020), (202), (11–3), (31–1), (220), (221), (22–2) planes of CuO (Chen et al. 2020; Liu
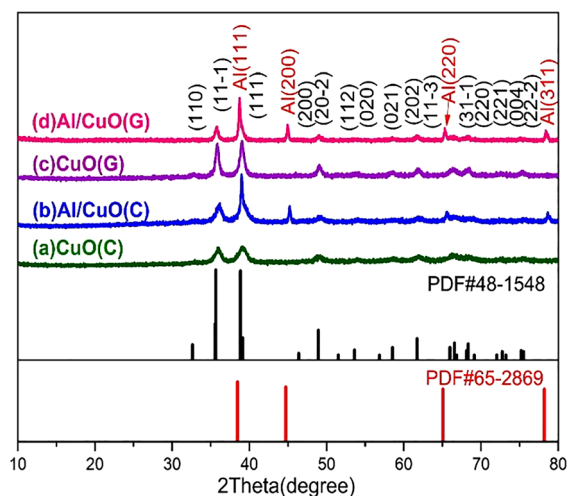
Fig. 1 XRD patterns of as-prepared catalysis

et al. 2020). CuO displayed weak diffraction peaks at 46.0°, 52.7°, 56.8°, and 75.1°, which could be assigned to the (200), (112), (021), (004) planes. All reflection peaks in Fig. 1a belonged to the monoclinic phase (space group C2/c(15)) with unit cell parameters $a = 4.6883$ Å, $b = 3.4229$ Å, $c = 5.1319$ Å, $\alpha = \gamma = 90°$, $\beta = 99.506°$ of CuO(C) (JCPDS No. 48–1548), which demonstrates its good purity. The signals et al. (111), Al (200), Al (220), and Al (311) corresponded to Al powders. All diffraction peaks in Fig. 1b matched with pure Al (JCPDS No. 65–2869) and CuO(C) (JCPDS No. 48–1548). The obvious characteristic diffraction peaks in Fig. 1c coincided with those given in the JCPDS card 48–1548 of CuO(G). The XRD pattern in Fig. 1d of Al/CuO(G) thermite

contained all Al and CuO diffraction peaks, thereby indicating that the crystal structures of Al and CuO were maintained during the sonication dispersion process.

The surface morphology and composition of the as-prepared CuO NPs were investigated using SEM, TEM, and EDS analyses. The SEM observations Fig 2a,b and high-resolution TEM image (HRTEM) Fig. 2c,d indicated that the as-prepared CuO sample displayed a crab cactus-like structure with a length of approximately 1.6 µm and an average diameter/breadth of approximately 1.0 µm in the middle portion of the structure. The enlargement of the local region (inset i in Fig. 2c) demonstrated each end of CuO with rough surfaces and boundaries. Generally, the crystallinity was poor in these areas, and crystal defects appeared. Figure 2e (inset iii) displays the stacking faults on the surface of CuO(C). CuO 3D hierarchical structure possessed single crystalline nature confirmed from the selected area electron diffraction (SAED) pattern in Fig. 2f. The EDS (Fig. 2g) results show that the product prepared was a pure CuO crystal, and the diffraction peak was obviously broadened, indicating that the crystal grain of the product was small. Determined from SEM (Fig. 2h, i) and TEM images (Fig. 2j, k), it was found that the as-prepared CuO NPs were characterized by their gypsophila paniculata-like structures and inhomogeneous grain size. The TEM micrograph in Fig. 2k suggested that the CuO NPs had rough surfaces due to the adhesion of small CuO spheres with an average particle diameter of 1.5 nm. A representative HRTEM image of CuO NPs is shown in Fig. 2l. It could be inferred that the gypsophila paniculata-like CuO structure was formed by the assembly of small particles. As shown in Fig. 2l, the distinct lattice fringe of 0.232 nm could be indexed to the (111) crystal plane of monoclinic CuO. The fast Fourier transform (FFT) pattern of the as-prepared CuO NPs is depicted in Fig. 2l (inset iv). Figure 2m presents the SAED pattern of CuO polycrystalline, which could be confirmed from the ring pattern diffraction. SEM-based EDS characterization identified that the gypsophila paniculata-like CuO contained Cu and O verified by obvious signal peaks (Fig. 2n).

SEM micrographs and TEM images in Fig. 3a, c suggested that CuO(C) NPs were tightly bound on the surface of Al NPs. As shown in Fig 3f, h, the gypsophila paniculata-like CuO(G) crystallites attached to the Al NPs uniformly, thereby preventing

the aggregation of Al and CuO(G) particles in the thermites. The HRTEM observation and FFT pattern of CuO(C) NP showed that the CuO(C) was a single crystal and grew along the (111) crystal plane (Fig. 3d and inset i). Similarly, the FFT pattern corresponding to the (111) plane of CuO(G) was observed in Fig. 3i, inset ii. Figure 3i, area "C" shows a high-resolution image of CuO(G) containing dislocation tangles/networks on the surface. The microstructure of the Al oxidized layer with a thickness within 0–3.5 nm was confirmed through HRTEM in Fig.3e, j. The chemical compositions of the two types of Al/CuO thermites were measured by the EDS analysis (Fig. 3b, g), which revealed Cu, O, and Al elements in the as-prepared Al/CuO thermite. The Cu and O elements originated from CuO crystallites whereas the Al element was obtained from the Al NPs.

Kinetic parameter, physical model and kinetic compensation effects

DSC curves of NC and CuO(C)-NC, Al/CuO(C)-NC, CuO(G)-NC and Al/CuO(G)-NC composites obtained at a heating rate of 10.0 K min^{-1} are presented in Fig. S1. Pure NC exhibited a strong exothermic peak at 209.67 °C, and the exothermic peak temperature decreased to 209.63 °C, 208.00 °C, 207.80 °C, and 207.53 °C with the addition of CuO(C), Al/CuO(C), CuO(G), and Al/CuO(G), respectively. Benefiting from the synergistic effect of Al powders and CuO particles, the catalytic activities of Al/CuO thermites were superior to that of pure CuO.

To explore the catalytic effects of CuO(C), Al/CuO(C), CuO(G), and Al/CuO(G) on the pyrolysis process of NC (Fig. S1) and obtain the corresponding kinetic parameters, the DSC curves with linear heating rates (Fig. 4) were analyzed using mathematics methods. From Fig. 4, the temperature increased with the heating rate, which indicated the effect of the heating rate on NC thermolysis, as in the previous reports (Tarchoun et al. 2019; Chai et al. 2019).

FWO, KAS, and Friedman isoconversional plots of CuO(C)-NC, Al/CuO(C)-NC, CuO(G) NC and Al/CuO(G)-NC in Fig. 5 were obtained from the simultaneous analysis (Sánchez-Jiménez et al. 2013) for the experimental plots shown in Fig. 4. The FWO isoconversional plot trend generally agreed with the KAS plot; also, it could be initially predicted that the obtained E_α values from the slopes of the straight lines
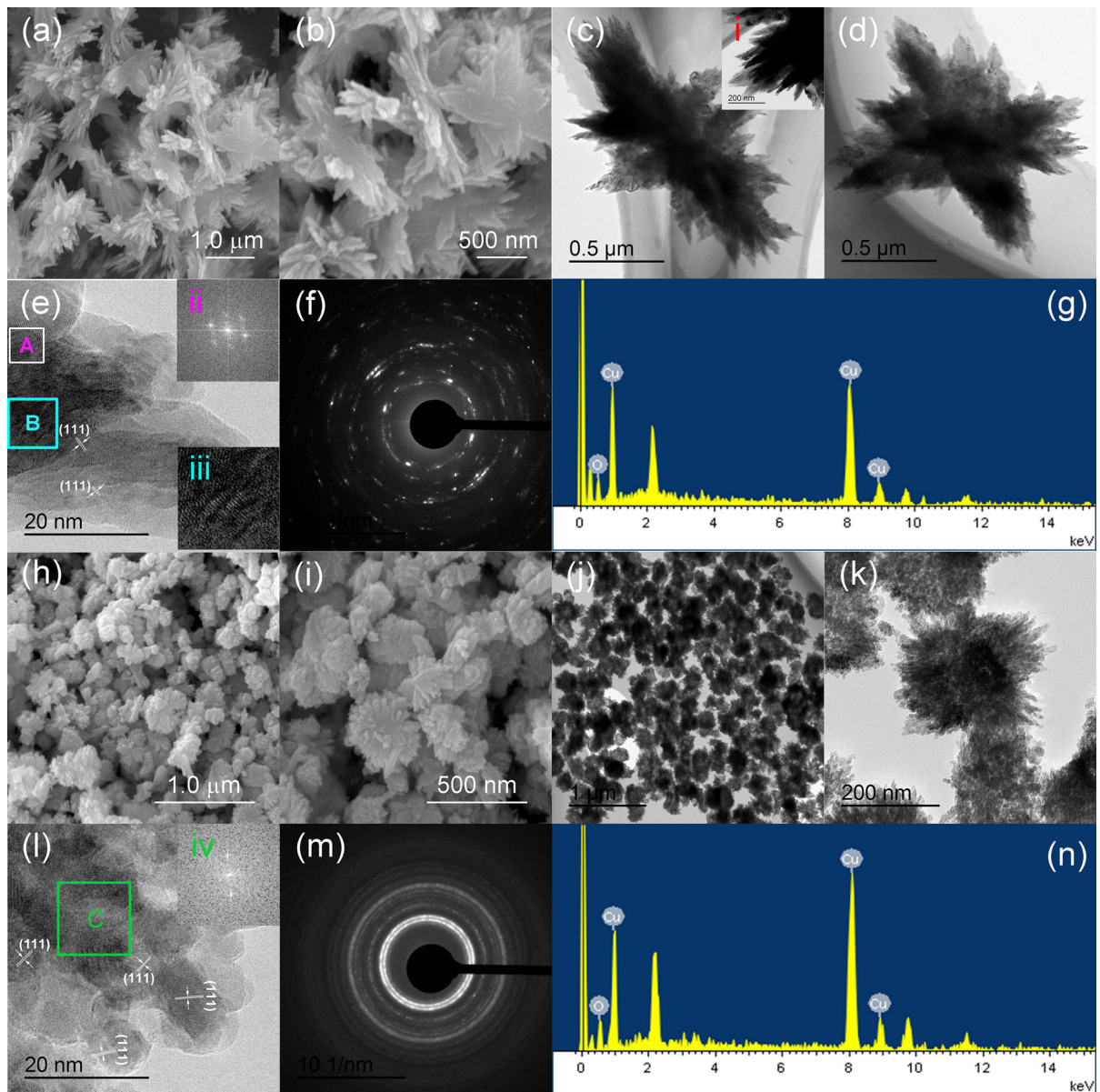
Fig. 2 **a**, **b** SEM micrographs and **c**, **d** low-magnification TEM images of CuO(C). Inset i is the TEM image of a small part of CuO(C) nanoparticle; **e** HRTEM image of CuO(C) nanoparticle. FFT pattern (inset, ii) marked "A" is attributed to [111] zone axis of CuO(C) crystal. Dislocation substructures (inset, iii) corresponding to the area "B" are observed; (**f**) SAED patterns of CuO(C) hierarchical structure; (**g**) EDS pattern of CuO(C); **h**, **i** SEM micrographs and **j**, **k** low-magnification TEM images of CuO(G); **l** HRTEM image of the small part of CuO(G) nanoparticle. FFT pattern (inset, iv) marked "C" correspond to [111] crystal plane of the monoclinic CuO(G); **m** SAED pattern of CuO(G) crystal; **n** EDS pattern of CuO(G)

in Fig. 5 seemed very close to each other for the same studied material. The Friedman isoconversional plot shows a slight difference trend due to the employed approximations (Xu et al. 2017) used in the algorithms. From Fig. 5, the lines ran approximately

parallel; however, the slopes of the lines corresponding to the high conversion rate (α) were varied. This variation of activation energy might be explained by the autocatalytic reactions of NC and the reactions between the intermediate products during
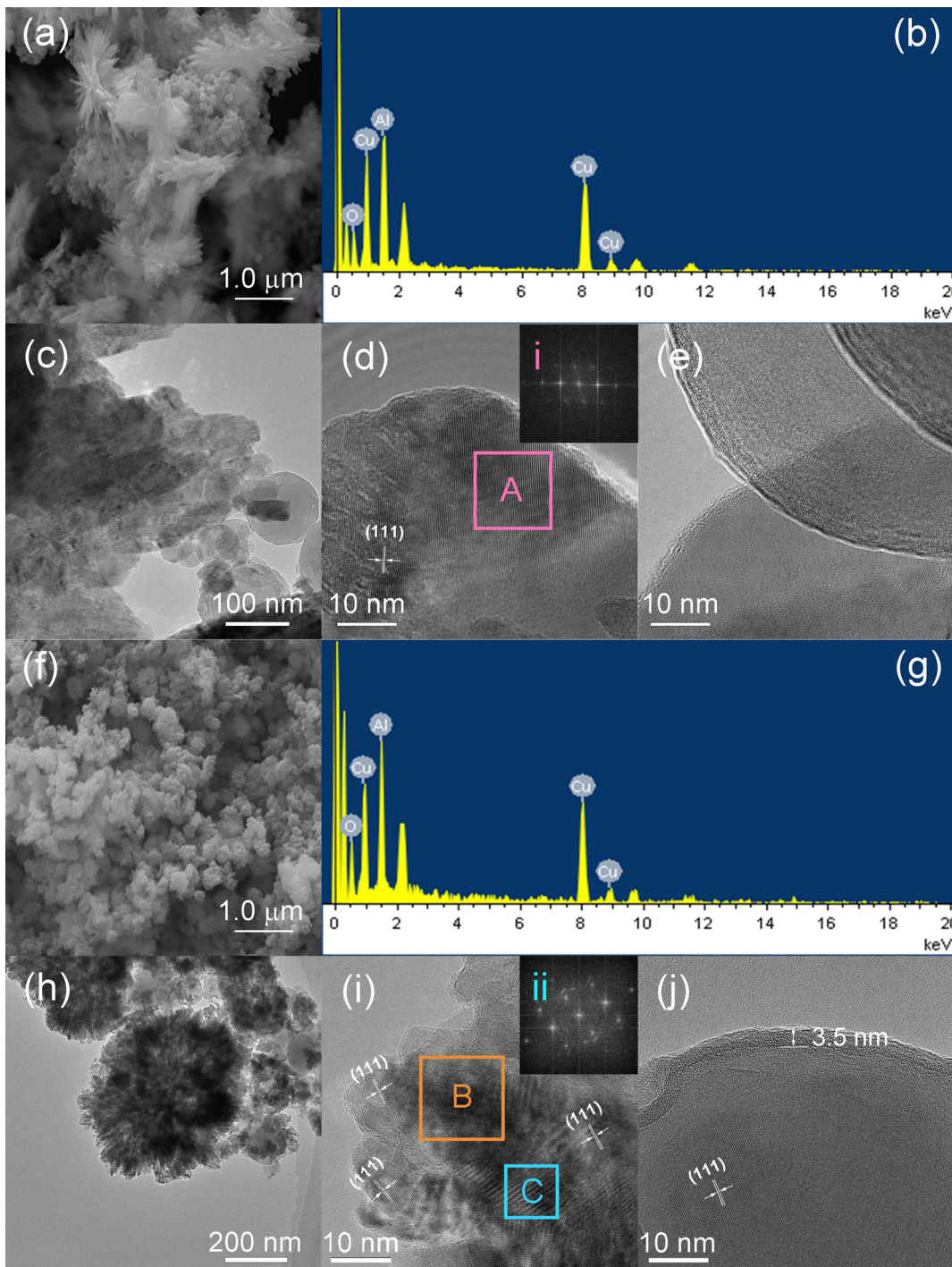
Fig. 3 **a** SEM micrograph, **b** EDS pattern and **c** TEM image of Al/CuO(C); **d** HRTEM image of CuO(C) nanoparticle. FFT pattern (inset, i) marked "A" is attributed to [111] zone axis of CuO(C); **e** HRTEM image of Al nanoparticle mixed with CuO(C); **f** SEM micrograph, **g** EDS pattern and **h** TEM image of Al/CuO(G); **i** HRTEM image of CuO(G) nanoparticle. FFT pattern (inset, ii) marked "B" is attributed to [111] zone axis of CuO(G). Dislocation substructures corresponding to the area "C" are observed; (**j**) HRTEM image of Al nanoparticle mixed with CuO(G)
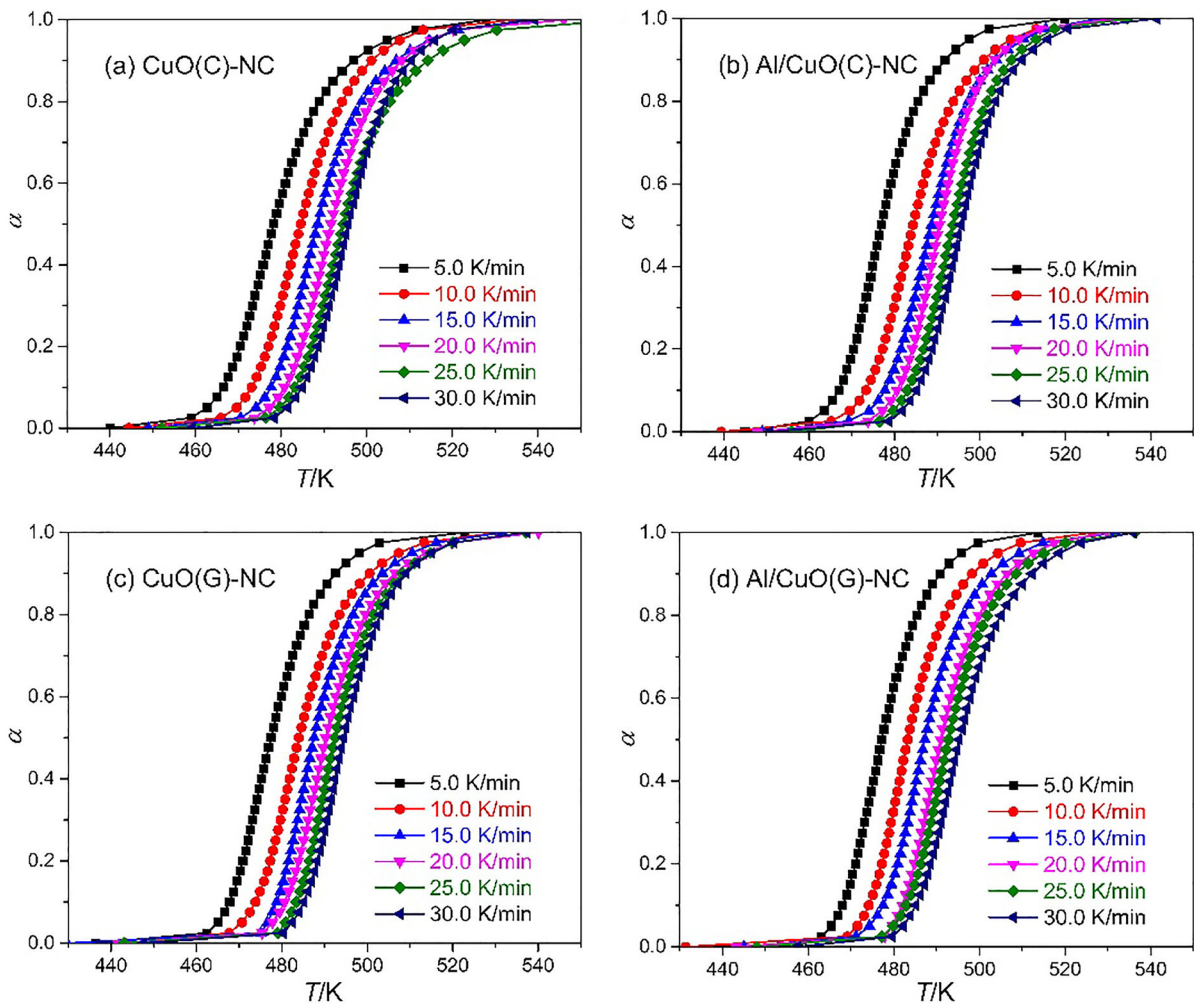
Fig. 4 Experimental plots obtained for the thermolysis of the NC-based composites in N_2 atmosphere with the linear heating rates

decomposition promoted by the catalysts (CuO and Al/CuO) and the strong oxidizing activity of gas products, such as NO_2.

By plotting $\ln(\beta_i)$, $\ln(\beta_i/T_{\alpha,i}^2)$, and $\ln[\beta_i(d\alpha/dT)_{\alpha,i}]$ against $1/T$ for α from 0.025 to 0.975 with a step-size of 0.025, the activation energies could be established by the slope (k) depending on $E_\alpha = -k\text{R}/1.052$ for FWO method, and $E_\alpha = -k\text{R}$ for KAS and Friedman methods. E_α and the related confidence intervals (errors bars) evolution with respect to α obtained using the KAS, FWO, and Friedman approaches are shown in Fig. 6. E_α obtained from DSC data almost agreed with calculations obtained using the FWO and KAS methods for the as-prepared NC-based composites. It could be seen that E_α obtained by Friedman

method exists some differences from those calculated by the other two model-free methods, which might be due to the accuracy of the mass loss derivative (Mamleev et al. 2004; Hadigheh et al. 2021). Compared with the E_α values of NC (Fig. S2), the E_α values of NC-based composites decreased due to autocatalytic characteristics of NC with the condition of 12.6% nitrogen content and the catalytic activity of catalysts during the initial reaction stage. As the conversion rate increased, the E_α values of the NC-based system with and without catalysts, including CuO(C), Al/CuO(C), and CuO(G), tended to increase, indicating a more complex chemical reaction. However, it revealed that the E_α values of Al/CuO(G)–NC first maintained a certain level and then decreases with the increase in conversion rates. In addition, the plots
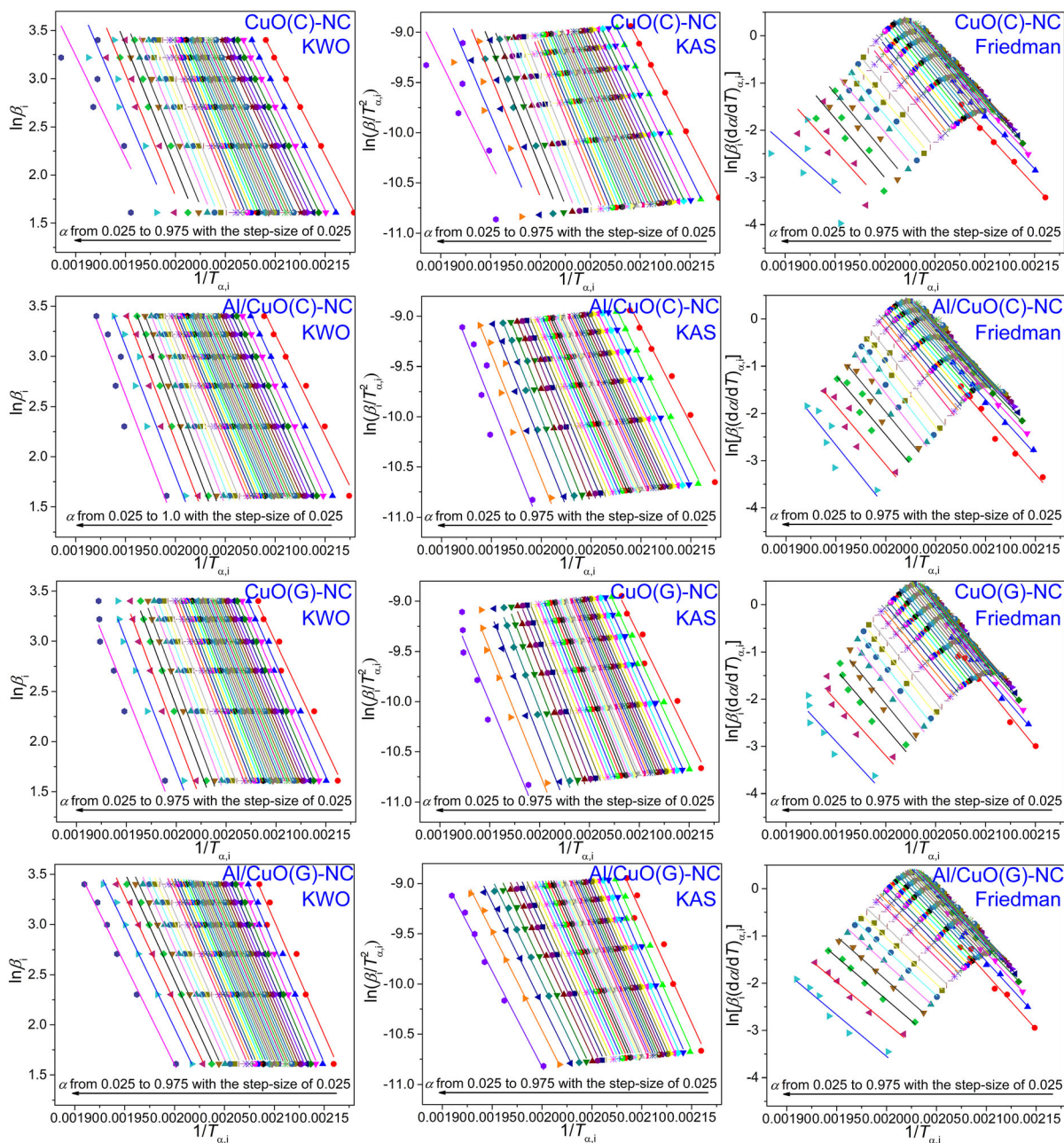
Fig. 5 Global kinetic plots of the NC-based composites depending on FWO, KAS and Friedman methods

for the above isoconversional methods exhibited comparable trends, and the obtained E_α values seemed to be close to each other. The results were obviously different from those of CuO(C)-NC, Al/CuO(C)-NC, and CuO(G)-NC composites, which were due to the different catalysis abilities of CuO(C), Al/CuO(C) and CuO(G), as well as the decomposition products.

Moreover, as presented in Table 1, the activation energy of Al/CuO(G)-NC decreased most significantly, indicating the best catalytic activity of Al/CuO(G) on the decomposition behavior of NC.

Figure 7 shows the theoretical curves for the kinetic models represented in Table S1 (García-Garrido et al. 2018; Sánchez-Jiménez et al. 2010), and experimental
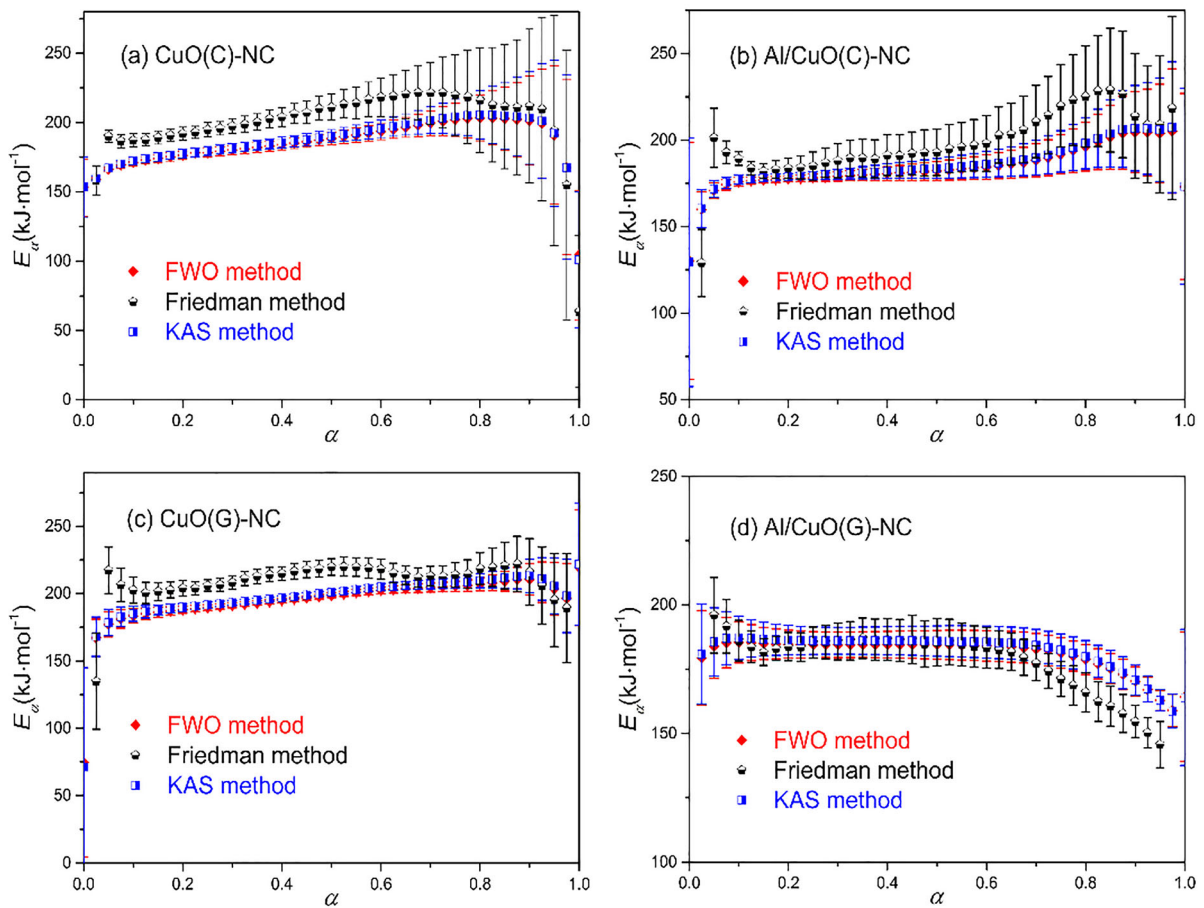
Fig. 6 E_α and the associated error evolution with respect to the conversion rate (α) obtained by the three employed isoconversional methods for the NC-based composites

Table 1 Kinetic parameters of decomposition reaction for NC-based composites

| Sample	Isoconversional method	E_α/(kJ mol^{-1})	lg(A/s^{-1})	Reconstructed model $f(\alpha)$
CuO(C)-NC	FWO	186.2 ± 6.2	19.5 ± 0.7	$9.314\alpha^{0.817}(1-\alpha)^{2.392}$
	KAS	187.7 ± 6.5	19.7 ± 0.7	
	Friedman	202.4 ± 9.3	21.4 ± 1.0	
Al/CuO(C)-NC	FWO	183.6 ± 7.2	19.2 ± 0.8	$7.792\alpha^{0.828}(1-\alpha)^{2.112}$
	KAS	185.1 ± 7.5	19.4 ± 0.8	
	Friedman	195.0 ± 12.5	20.7 ± 1.4	
CuO(G)-NC	FWO	196.5 ± 4.7	20.5 ± 1.6	$8.474\alpha^{0.713}(1-\alpha)^{2.335}$
	KAS	198.4 ± 4.5	20.7 ± 1.6	
	Friedman	212.1 ± 7.2	22.5 ± 0.8	
Al/CuO(G)-NC	FWO	181.2 ± 7.2	19.1 ± 0.7	$7.367\alpha^{0.732}(1-\alpha)^{2.145}$
	KAS	182.5 ± 6.2	19.2 ± 0.7	
	Friedman	177.6 ± 7.3	18.9 ± 0.8	
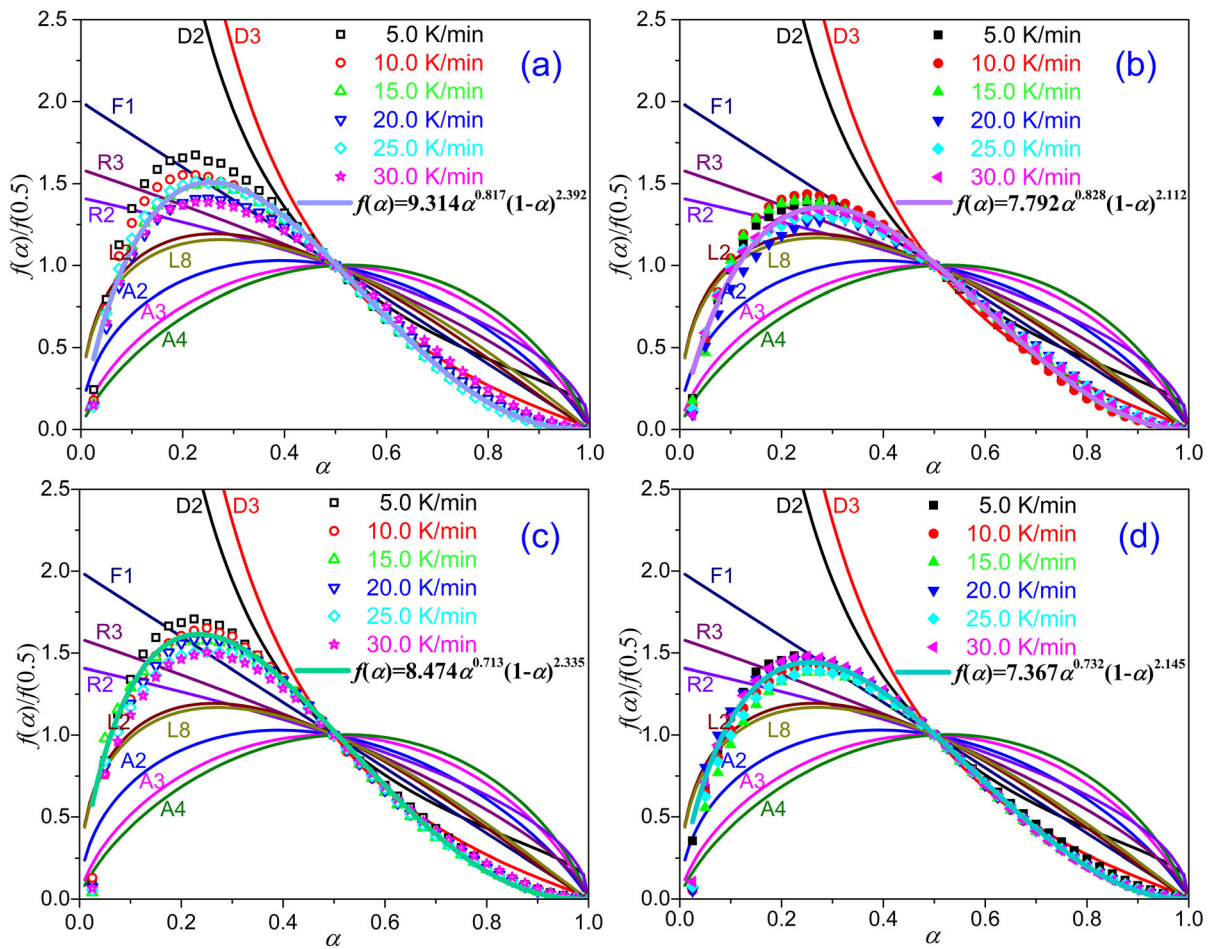
Fig. 7 Comparison between normalized curves of the reaction models for **a** CuO(C)-NC, **b** Al/CuO(C)-NC, **c** CuO(G)-NC and **d** Al/CuO(G)-NC and theoretical master curves established from the ideal reaction models in Table S1

master curves were drawn based on the experimental data from the curves in Fig. 4. The experimental master curves obtained at six heating rates should run similar trends, while cannot be fitted well with any theoretical curve. The reason was that the commonly used models listed in Table S1 were single step reaction models, which were unsuitable for pyrolysis reactions in solid or porous structural solids including the complex multistep pyrolysis reaction of NC. So, the experimental data reconstruction had bad repetitions when the formula assumed as the best fitting kinetic reaction model was chosen from Table S1. That is, even the selected highly fitting model was not a true model of NC pyrolysis (Gao et al. 2019). Therefore, an adjustment function—the modified Šesták–Berggren empirical equation (Eq. (1))—was introduced to reconstruct the reaction model based on

the combined kinetic analysis method to be highly compatible with the experimental data. Equation (1) was proved to be fit for every ideal kinetic model in Table S1 by only modifying the proper c, m, and n parameters to span the most common physical models and their possible deviations from ideal conditions (Pérez-Maqueda et al. 2006; Zhongliang et al. 2019).

$$f(\alpha) = c\alpha^m(1 - \alpha)^n \tag{1}$$

By analyzing the experimental data in Fig. 8 and matching works, the relation curves of the four NC-based composites were obtained from the experiments by which we could obtain rational c, n, and m values and finally realized the reaction models. The reaction model functions of the four NC-based composites could be expressed as quantitative relation formulas (Table 1) (Fig. 8a–d), respectively. The kinetic
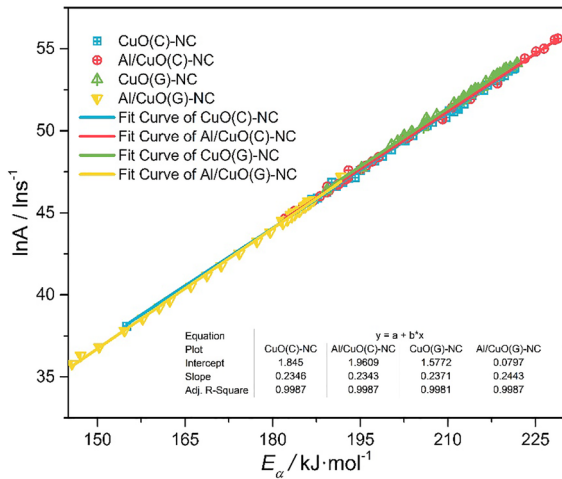
Fig. 8 The energy compensation effect for pyrolysis of the NC-based composites calculated via the combined kinetic analysis method

compensation effect described a linear relationship between E_α and the pre-exponential factor. The better the correlation, the more rational the reaction model. The modified theoretical models were in high accordance with the corresponding experimental data (Fig. 9). From Fig. 9, the slopes and intercepts corresponding to four straight lines varied, indicating that CuO(C), Al/CuO(C), CuO(G), and Al/CuO(G) catalytically influenced on the compensation effect parameters of NC differently. Based on the numerical model reconstruction, the pyrolysis processes of CuO(C)-NC, Al/CuO(C)-NC, CuO(G)-NC and Al/CuO(G)-NC could be controlled mainly by the modified *n*-order reaction models. A similar integral reaction model has already been reported for pure NC (Gao et al. 2019). In fact, various reaction models and Arrhenius parameters of NC with or without catalysts have been reported (Benhammada and Trache 2021; Benhammada et al. 2020a, b; Tarchoun et al. 2020c),
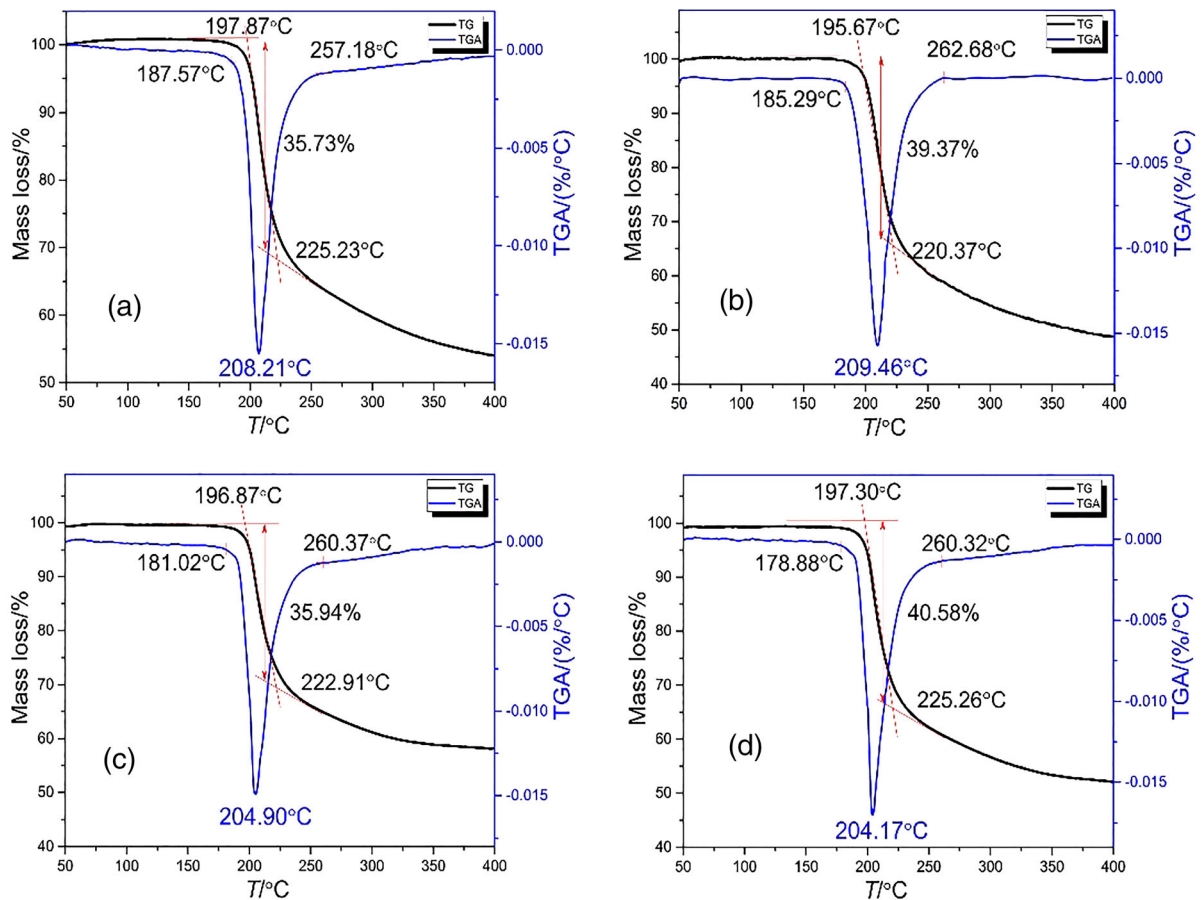
Fig. 9 TG-TGA curves of **a** CuO(C)-NC, **b** Al/CuO(C)-NC, **c** CuO(G)-NC and **d** Al/CuO(G)-NC

which could be explained by the difference in the nitrogen content of NC (Pourmortazavi et al. 2009), employed analytical techniques, kinetics methods (Chelouche et al. 2019), and catalyst characteristics.

TG-FTIR analysis

The TG-FTIR is an established technique for exploring the pyrolysis process of high energy density materials. Figure 9 shows the TG-TGA curves of NC-based composites under a heating rate of 10 K min^{-1} within 50–400 °C. A single-stage decomposition was noticed in the TG curves of CuO(C)-NC, Al/CuO(C)-NC, CuO(G)-NC, and Al/CuO(G)-NC composites; the weight losses were 35.73%, 39.37%, 35.94%, and 40.58%, respectively. Compared with the weight loss of NC (68.41%) reported by us (Zhao et al. 2016a), the weight loss of the composites reduced after the addition of the catalyst. The undecomposed remains were attributed to the NC residues, CuO catalyst or products of the aluminothermic reaction. As the TG-TGA curves of CuO(C)-NC in Fig. 9a shown, starting temperature of pyrolysis (T_i), temperature of extrapolated onset (T_e), temperature of maximum pyrolysis rate (T_p), extrapolated final temperature (T_c), and terminal temperature (T_f) of the thermal decomposition process were 187.57 °C, 197.87 °C, 208.21 °C, 225.23 °C and 257.18 °C. Figures 9b–d show the representative temperatures (T_i, T_e, T_p, T_c, and T_f) for Al/CuO(C)-NC, CuO(G)-NC and Al/CuO(G)-NC, respectively. As in our previous report on NC pyrolysis (Zhao et al. 2016b), the T_e and T_p of the composites were lower than these of NC due to the addition of catalysts, which agreed with the DSC results. The pyrolysis behaviors and products of the four NC-based composites should be proposed, and the catalytic mechanism of the catalyst should be revealed.

According to previous studies (Benhammada et al. 2020a, b; Katoh et al. 2010; Trache et al. 2017), including our reports (Zhao et al. 2016c), the pyrolysis process of NC starts from the rupture of the –O–NO$_2$ bond, and the released N$_2$ stands still within the polymeric compound, then reacts with the free radical or thermally degraded products. In addition, we found that Fe$_2$O$_3$ NPs, as catalysts, could promote the breaking of –O–NO$_2$ bonds and keep the gaseous products stagnant within the polymeric skeleton

attributed to superior adsorption capacity, thus accelerating autocatalysis.

The catalysts investigated in this study had a wide variance between the Fe$_2$O$_3$ NPs. The TG-FTIR technique was employed to investigate the pyrolysis processes of the four as-prepared NC-based composites. Figures 10 and S3 show IR spectra of gas products at various representative temperatures, including T_i, T_e, T_p, T_c, and T_f. To determine whether H$_2$O and CO$_2$ came from the environment or from the thermal decomposition process, the IR spectra at a certain temperature point (T_x) before the initial decomposition temperature was considered for a the comparative study.

The IR characteristic absorption peaks of CuO-NC at 165.30 °C (T_x) and 187.57 °C (T_i) are shown in Figs. 10a and S3(a). H$_2$O (3605–3741 cm^{-1}), CO$_2$ (2365, 672 cm^{-1}), and NO$_2$ (1592–1636 cm^{-1}) (Li et al. 2012; Wang et al. 2016) could be confirmed. These results were different from the initial stage of the thermal decomposition of NC, which did not decompose to generate NO$_2$ before the initial decomposition temperature. Although NC might slowly decompose as temperature increased, it was enhanced by CuO(C) particles due to their catalysis. The peaks at 3605–3741 cm^{-1} could be attributed to the O–H bonding vibration of H$_2$O. The bands at 2360 and 670 cm^{-1} were assigned to the stretching and bending vibration modes of CO$_2$, respectively. By comparing the IR spectra at 165.30 °C (T_x) and 187.57 °C (T_i) in Fig. 10a, the intensities of the discovered H$_2$O, CO$_2$ and NO$_2$ were almost invariant. At 197.87 °C (T_e), the absorption peaks of H$_2$O, CO$_2$, NO$_2$, and N$_2$O (2241 cm^{-1}) were easily identifiable (Fig. 10a, T_e). When the temperature increased to 208.21 °C, the gaseous products including NO (1763–1966 cm^{-1}), CO (2195 cm^{-1}), N$_2$O (2240 cm^{-1}), HCHO (2815, 1741 cm^{-1}), and HCOOH (1081–1129 cm^{-1}) were detected (Gratien et al. 2007). The bands at 2815 and 1741 cm^{-1} associated with the C–H and C=O stretching vibration of HCHO due to the cleavage of the $-$CH$_2$ONO$_2$ groups (Chen et al. 1991). The HCOOH gas products resulted from the secondary self-catalyzed reactions of NC (Shehata et al. 2003). The gas product HCN (2240–2260 cm^{-1}) might be generated by the reaction of HCO$\bullet$ radical with NO (Wei et al. 2010). From Fig. 10 (a, T_p), the strength of these gases was significantly enhanced, which was an essential basis for the faster pyrolysis rate of CuO(C)-
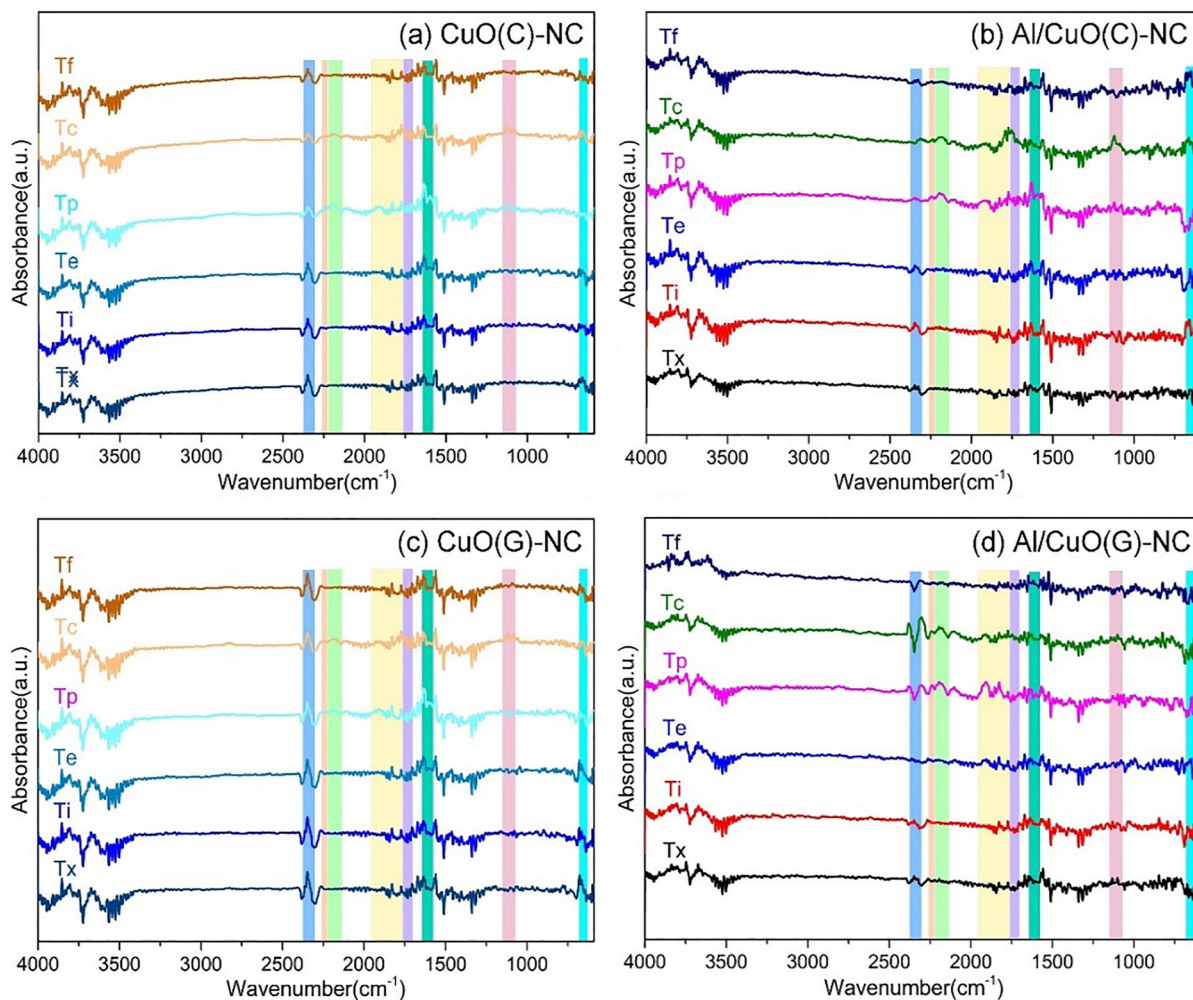
Fig. 10 IR spectra of the gases evolved from the degradation of the NC-based composites

NC complex than that of the pristine NC, and showed the catalytic effect of CuO(C) particles. The CuO(C) particles exist rough surfaces and lattice defects (Fig. 2), which could provide adsorption and active sites to absorb the gases produced during the pyrolysis process of NC, thereby promoting a secondary autocatalytic reaction. At 225.23 °C (T_c), the intensities of NO_2, N_2O, HCHO and CO were weak compared with the plots in Fig. 10(a, T_p and T_c). The intensities of CO_2, NO, HCOOH and H_2O increase might be due to the remaining thermolysis or the reaction of NO_2 and HCHO (Wei et al. 2010) with the catalysis of CuO(C) particles. At the final stage of the decomposition (Fig. 10a, T_f), the peaks of HCOOH, NO and CO disappeared, and the NO_2, CO_2 and H_2O gases were still detected.

Because commercial NC is accompanied by unstable impurities (such as residual acid, cellulose sulfate, nitro-sulfur mixed esters, and various nitro-sugars) during the manufacturing process, these unstable impurities are easily decomposed. The catalysis of decomposition products and the autocatalytic decomposition of NC could promote NC pyrolysis. Although the NC used in the experiment has high purity, NC was also hydrolyzed due to the presence of a catalyst at high temperatures. The hydrolysis products promoted the further decomposition of NC, and the autocatalytic process was repeated. With the Al/CuO(C) catalyst, the gas products H_2O, CO_2 and NO_2 were detected from the IR spectrum of Al/CuO(C)-NC at 165.30 °C (T_x) (Figs. 10b and S3(b)). At the initial decomposition temperature (T_i = 185.29 °C) of Al/CuO(C)-NC,

the IR characteristic peaks of H_2O, CO_2, NO_2 and NO could be identified. At 195.67 °C (T_e), the intensities of absorption peaks including H_2O, CO_2, NO_2, and NO are slightly increased. It can be mentioned that more gases were released at 209.46 °C (T_p), containing H_2O, CO_2, NO_2, NO, N_2O (2200–2300 cm^{-1}), CO, HCN (2240–2260 cm^{-1}), $HCHO$ (2700–2900 cm^{-1}), and $HCOOH$. The intensities of NO_2, N_2O, CO_2, CO, HCN, and $HCOOH$ peaks increased with temperature. The peak of $HCHO$ was weak, probably due to the reaction between NO_2 and $HCHO$. The decrease in $HCHO$ gas might be due to the addition of Al/CuO(C) catalyst hindering the thermal decomposition of the $–CH_2O\bullet$ groups. At 220.37 °C (T_c), the peaks of $HCOOH$, NO, and CO_2 were found to be stronger than the others, and the peaks of H_2O, NO_2, N_2O, CO, HCN, $HCHO$ were detected. Additionally, the distinguishable IR bands of H_2O, CO_2, NO_2 and $HCOOH$ were detected at the final temperature ($T_f = 262.68$ °C) of the decomposition process of Al/CuO(C)-NC. From the escaped gas products, the catalytic action of Al/CuO(C) was different from that of CuO(C). It can be concluded that the Al/CuO(C) interacted with NC during the catalytic process to generate metal atoms or clusters of "active species" with high catalytic activity, and immediately participated in the catalytic reaction, thereby maximizing the catalytic performance of the catalyst.

For the IR data of CuO(G)-NC at 165.30 °C, the bands in the range of 3557–3739 cm^{-1} could be attributed to the O–H bond. The obvious IR bands of CO_2, NO, and NO_2 were presented at 2306–2383 cm^{-1}, 1771–1889 cm^{-1} and 1571–1639 cm^{-1}, respectively. At 181.02 °C, the peaks of H_2O, CO_2, NO and NO_2 are detected from the IR spectrum of CuO(G)-NC (Figs.10c and S3(c)). At 196.87 °C, more gas phase products such as H_2O, CO_2, NO, $HCHO$, $HCOOH$ and NO_2 were identified. At 204.90 °C, CuO(G)-NC exhibited characteristic bands in the ranges of 3500–3731 cm^{-1}, 2725–2920 cm^{-1}, 2296–2384 cm^{-1}, 2241 cm^{-1}, 2240–2260 cm^{-1}, 2145–2196 cm^{-1}, 1771–1932 cm^{-1}, 1563 ∼ 1634 cm^{-1} and 1109 cm^{-1} that corresponded to H_2O, $HCHO$, CO_2, N_2O, HCN, CO, NO, NO_2, and $HCOOH$, respectively. The bands of N_2O, HCN, CO, NO, and NO_2 were much stronger at the temperature range from 196.87 °C to 204.90 °C. Otherwise the bands of CO_2 and $HCOOH$ gradually weakened after the CuO(G)-

NC composites started to decompose. From Fig. 10c, the signals of H_2O (3506–3723 cm^{-1}), $HCHO$ (2786–2858 cm^{-1}), CO_2 (2300–2383 cm^{-1}), N_2O (2241 cm^{-1}), HCN (2236–2254 cm^{-1}), CO (2108–2201 cm^{-1}), NO (1767–1932 cm^{-1}), NO_2 (1569–1628 cm^{-1}), and $HCOOH$ (1056–1133 cm^{-1}), corresponding to the IR spectrum of CuO(G)-NC at 222.91 °C, could be observed, whereas the content of NO_2 gradually decreased, and the absorbance intensities of gaseous products including $HCHO$, N_2O, HCN, CO, NO, and $HCOOH$ increased with temperature. At 260.37 °C, peaks were revealed in the ranges of 3505–3736 cm^{-1}, 2301–2384 cm^{-1}, 1771–1900 cm^{-1}, 1565–1647 cm^{-1}, and 1068–1133 cm^{-1} corresponding to H_2O, CO_2, NO, NO_2 and $HCOOH$, respectively. The thermolysis process of CuO(G)-NC started from the rupture of the $–O–NO_2$ bond and released NO_2. With the fracture of the $–C–O–C–$ bond, the skeleton of the NC macromolecule collapsed. Owing to the catalytic action of CuO(G), the escaping NO_2 gas was confined in the skeleton and further reacted with the condensed phase, triggering a self-catalytic reaction, thus accelerating the decomposition of NC and producing H_2O, $HCHO$, CO_2, N_2O, HCN, CO, NO, NO_2, and $HCOOH$.

Figures 10d and S3(d) present the IR spectra of Al/CuO(G)-NC at typical temperatures in the N_2 atmosphere. At 165.30 °C, the peaks of H_2O, CO_2 and NO_2 were assigned. At 178.88 °C, the main evolved gases during the Al/CuO(G)-NC thermolysis are H_2O, $HCHO$, CO_2, NO, and NO_2. The peaks at 197.30 °C were due to the evolution of H_2O, CO_2, $HCHO$, N_2O, HCN, CO, NO_2, NO, and $HCOOH$ gases. By comparing the IR spectra of 197.30 °C and 204.17 °C, the type of the evolved gas was unchanged, but the intensities of the absorption peaks of CO_2, N_2O, HCN, CO, and NO gases significantly increased. At 225.26 °C, the H_2O, $HCHO$, CO_2, N_2O, CO, NO, NO_2, and $HCOOH$ absorption peaks existed, whereas the intensities of CO_2, CO, and $HCOOH$ increased, and the peak of $HCHO$ decreased. At the final stages of the decomposition, the gaseous products of Al/CuO(G)-NC mainly contained H_2O, CO_2, NO, NO_2, and $HCOOH$. Overall, after adding of Al/CuO(G), the gaseous small molecules remarkably increased, which revealed that the pyrolysis of Al/CuO(G)-NC composite was more complete at the existence of Al/CuO(G).

Based on the TG-FTIR experiment analysis above, the pyrolysis mechanism of the four NC-based composites could be deduced by Scheme S1. During the NC thermolysis, the –O–NO$_2$ bonds first ruptured and released NO$_2$, which was much obvious with the presence of catalysts at high temperatures. The glucopyranosyl ring might further be cleaved to produce H$_2$O, CO$_2$, and NO gases. These gaseous products, especially NO$_2$, could react with the condensed phase, free radical, and other products generated from the polymer degradation. CuO(C), Al/CuO(C), CuO(G), and Al/CuO(G) could accelerate the autocatalytic reaction of NC and produce H$_2$O, CO$_2$, N$_2$O, HCN, CO, NO, NO$_2$, HCHO, and HCOOH.

Catalytic combustion property of AP/HTPB propellants

Figure 11 shows 3D histograms of burning rate versus pressure (Brewster and Mullen 2011) and catalytic efficiency versus pressure of AP/HTPB propellants. From Fig. 11a, the burning rate of the blank group (N0) and experimental groups (C1, C2, T1, and T2) increased with an increase in pressure in the range of 4–15 MPa. At 15 MPa, all formulations (N0, C1, C2, T1, and T2) had the fastest combustion rate and highest catalytic efficiency. For all groups, both the burning rates and catalytic efficiencies within 4–15 MPa followed the order: N0 < C1 < T1 < C2 < T2. Compared with N0, the burning rate of C1, C2, T1, and T2 containing CuO(C), CuO(G), Al/CuO(C), and Al/CuO(G) catalysts at 15 MPa increased by 11%, 17%, 23%, and 43%, respectively. The catalytic efficiencies of C1, C2, T1, and T2 at

15 MPa were 11%, 17%, 23%, and 43% higher than that of N0. The results meant that the catalytic capability of Al/CuO(G) was the best of all catalysts. Thermites had higher catalytic activity than oxides; for the thermites, the catalytic activity was in the order: Al/CuO(C) < Al/CuO(G); for the oxides, the order was CuO(C) < CuO(G) (within 4–15 MPa).

From the above experimental results, the burning rate exhibited greater sensitivity to the pressure. The ensuing flow oscillations occurring in the interior of a solid rocket motor substantially increase the pressure, which can further influence the instantaneous combustion rate. However, excessive pressure will cause the solid rocket motor to crack. The exponent (n) of propellants was another significant parameter that impacted the chamber pressure. To avoid causing large variations in thrust or combustion chamber in a high pressure environment, the pressure exponent should be as small as possible. In most situations, the n value of composite solid propellant was in the range of 0.2–0.65. Notably, that the n value was also related to the species and composition of the propellant formulations, such as the burning rate modifiers/catalysts. From Fig. 12, the data show that the pressure exponents of C1, C2, T1, and T2 with catalysts were lower than that of N0 in different pressure ranges. The formulations containing CuO(G) possessed lower pressure exponents than the formulations containing CuO(C), especially in the high pressure range. For the formulations including thermite, the pressure exponent of T2 was much smaller than that of T1 within 7–15 MPa.

Consequently, the burning performances of AP/HTPB propellants only depended on the catalyst;
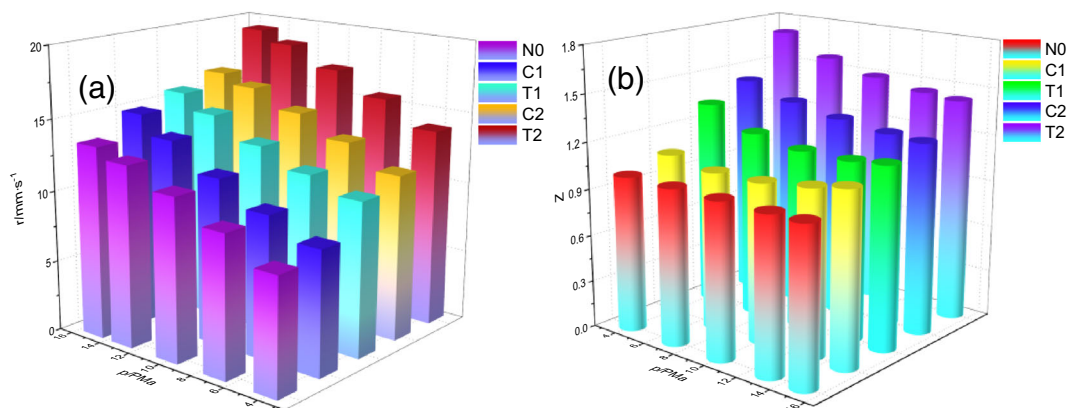
Fig. 11 Burning rate (r) **a** and efficiency **b** vs pressure (p) 3D histograms of AP/HTPB propellants
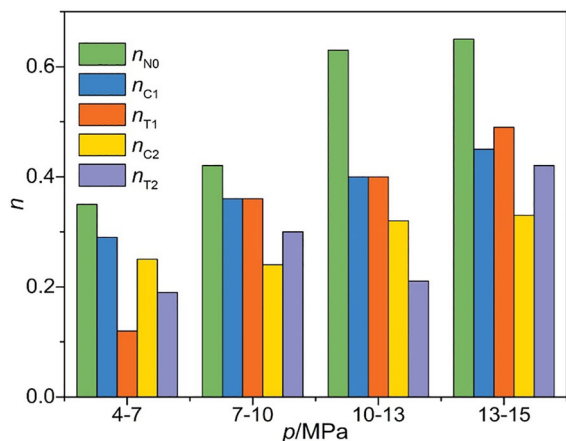
Fig. 12 Pressure exponent (n) of propellant formulations at different pressures

when the kind and composition of a formulation is determined, with the exception of catalyst. T2 exhibited the fastest burning rate, highest catalytic efficiency, and most rational pressure exponent when the Al/CuO(G) catalyst was added. Thus, Al/CuO(G) was the best catalyst. Because the Al powder used in the thermites was the same, the catalysis of the thermite was explained by the CuO particles with different morphologies.

To assess the catalytic combustion of the as-prepared CuO NPs, the S_{BET}, pore volume, and average pore diameter of CuO NPs were carried out. Both CuO(C) and CuO(G) exhibited a type IV physisorption isotherm Fig. 13a in accordance with the International Union of Pure and Applied

Chemistry (IUPAC) classification (Sing et al. 1985; Thommes et al. 2015), which was characteristic of mesoporous materials. The specific surface area was evaluated to be 48.93 and 90.14 m^2 g^{-1} for CuO(C) and CuO(G), respectively. Compared with CuO(C), the specific surface area of CuO(G) increased by 41.21 m^2 g^{-1}, which suggested that CuO(G) particles exhibited the mesoporous structure and provided more adsorption and active sites. For CuO(C), there was a slight increase in the adsorption capacity values in the high-pressure region (P/Po) of type H3 hysteresis loop, due to nitrogen capillary condensation in a stochastic and interconnected pore network. The pore diameter distribution of CuO(C) indicated the pore size distribution in the mesoporous region with an average pore diameter of ca. 9.1 nm (Fig. 13b). CuO(G) exhibited a type H4 hysteresis loop judging by the IUPAC classification, revealing the existence of narrow pores with the maximal pore size of about ca. 4.3 nm. The total pore volumes of CuO(C) and CuO(G) were 0.066 and 0.046 cm^3 g^{-1}, respectively. The results indicated that there were ultrananopores in mesoporous nanomaterials, which are seen in the TEM image (Fig. 2k).

Solid-state reactions often occur between crystal lattices or with molecules and may depend on lattice defects. The catalyst with crystal defects and high specific surface area (Yu et al. 2019) will accelerate the bond breaking and the release of small molecular fragments. The specific surface area of CuO(G) was much larger than that of CuO(C). The mesoporous structure, rough surfaces and ultrananopores provided
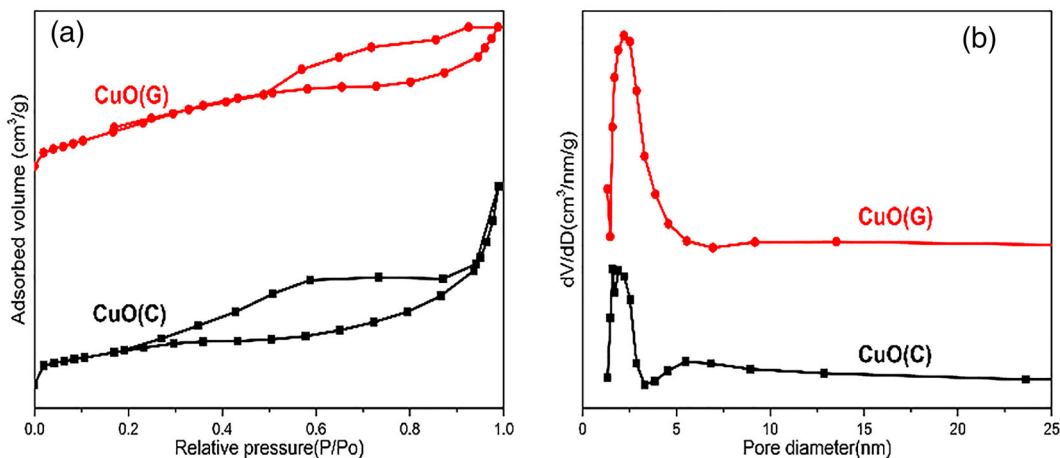
Fig. 13 Nitrogen adsorption–desorption isotherms **a** and pore size distribution curves **b** of CuO structures

more adsorption positions and active sites, which were favorable for the activation and diffusion of the reactants, thereby enhancing the thermal and combustion catalytic properties of CuO(G).

Conclusion

Structure-catalytic activity relationships of CuO particles and their particle size/shape dependencies on the catalytic thermal degradation of NC as well as the catalytic combustion performance of AP/HTPB propellant were investigated in this study. Gypsophila paniculata- and crab cactus-like CuO structures were successfully obtained by hydrothermal methods and integrated with Al powders to achieve Al/CuO thermite via ultrasonic mixing. The as-prepared CuO and Al/CuO thermites are promising catalysts in reducing the activation energy and the peak temperature of NC thermolysis. With these catalysts, strong catalytic effects occurred, promoting the $-O-NO_2$ bond cleavage during the initial pyrolysis of NC, as well as the condensed-phase decomposition and the reactions between the intermediate products. The initial heat release process of NC follows a certain autocatalytic decomposition reaction, whereas its mechanism model changes to fit well with the n-th order reaction at high- temperature ranges. In addition, the proper $f(\alpha)$ of NC-based composites were determined by model reconstruction with a modified Šesták–Berggren empirical equation based on the combined kinetic analysis method. TG-FTIR analysis certified that the thermolysis mechanism of NC could be changed by mixing different catalysts, which could have resulted from the absorption and desorption procedure of gaseous products generated within the range of different temperatures on catalysts with various adsorption positions and active sites. The burning rate of the formulation containing catalysts Al/CuO(G) increased by 43% compared with the basic formulation without catalyst at 15 MPa due to the large specific surface area ($90.14 \ m^2 \ g^{-1}$) for CuO(G) and the addition of Al nanopowders. This study presents two potential catalysts, including CuO particles and their corresponding thermites, by investigating the relationship of microstructure and catalytic activity; and gives a promising way to choose an excellent catalyst for accelerating the pyrolysis process of NC and improving the combustion performance of AP/HTPB composite propellants.

Declarations

Conflict of interest The authors declare that they have no conflict of interest.

References

An T, Zhao FQ, Pei Q, Xiao LB, Xu SY, Gao HX, Xing XL (2011) Preparation, characterization and combustion catalytic activity of nanoparticle super thermites. Chinese J Inorg Chem 27:231–238. https://doi.org/10.3969/j.issn.1001-4861.2013.00.020

Benhammada A, Trache D (2020) Thermal decomposition of energetic materials using TG-FTIR and TG-MS: a state-of-the-art review. Appl Spectrosc Rev 55(8):724–777. https://doi.org/10.1080/05704928.2019.1679825

Benhammada A, Trache D (2021) Green synthesis of CuO nanoparticles using *Malva sylvestris* leaf extract with different copper precursors and their effect on nitrocellulose thermal behavior. J Therm Anal Calorim. https://doi.org/10.1007/s10973-020-10469-5

Benhammada A, Trache D, Kesraoui M, Chelouche S (2020a) Hydrothermal synthesis of hematite nanoparticles decorated on carbon mesospheres and their synergetic action on the thermal decomposition of nitrocellulose. Nanomaterials 10(5):968. https://doi.org/10.3390/nano10050968

Benhammada A, Trache D, Kesraoui M, Tarchoun AF, Chelouche S, Mezroua A (2020b) Synthesis and characterization of α-Fe_2O_3 nanoparticles from different precursors and their catalytic effect on the thermal decomposition of nitrocellulose. Thermochim Acta 686:178570. https://doi.org/10.1016/j.tca.2020.178570

Botelho FD, Galante E, Mendes Á, José B (2015) Characteristics and manufacture of spherical smokeless powders. J Aerosp Technol Manag 7(4):398–403. https://doi.org/10.5028/jatm.v7i4.466

Boulkadid MK, Lefebvre MH, Jeunieau L, Dejeaifve A (2019) Burning rate of artificially aged solid double-base gun propellants. J Energ Mater 38(2):1–19. https://doi.org/10.1080/07370652.2019.1657204

Brewster MQ, Mullen JC (2011) Burning-rate behavior in aluminized wide-distribution AP composite propellants. Combust Explos Shock Waves 47(2):200–208. https://doi.org/10.1134/S0010508211020092

Chai H, Duan Q, Jiang L, Gong L, Chen H, Sun J (2019) Theoretical and experimental study on the effect of nitrogen content on the thermal characteristics of nitrocellulose under low heating rates. Cellulose 26(2):763–776. https://doi.org/10.1007/s10570-018-2100-0

Chajistamatiou AS, Bakeas EB (2016) A rapid method for the identification of nitrocellulose in high explosives and smokeless powders using GC–EI–MS. Talanta 151:192–201. https://doi.org/10.1016/j.talanta.2016.01.038

Chaturvedi S, Dave PN (2019) Solid propellants: AP/HTPB composite propellants. Arab J Chem 12(8):2061–2068. https://doi.org/10.1016/j.arabjc.2014.12.033

Chelouche S, Trache D, Tarchoun AF, Khimeche K (2019) Effect of organic eutectic on nitrocellulose stability during artificial aging. J Energ Mater 37(4):387–406. https://doi.org/10.1080/07370652.2019.1621407

Chen JK, Brill TB (1991) Thermal decomposition of energetic materials. 50. Kinetics and mechanism of nitrate ester polymers at high heating rates by SMATCH/FTIR spectroscopy. Combust Flame 85:479–488. https://doi.org/10.1016/0010-2180(91)90149-6

Chen Y, Ren W, Zheng Z, Wu G, Hu B, Chen J, Wang J, Yu C, Ma K, Zhou X, Zhang W (2020) Reactivity adjustment from the contact extent between CuO and Al phases in nanothermites. Chem Eng J 402:126288. https://doi.org/10.1016/j.cej.2020.126288

Dai J, Xu J, Wang F, Tai Y, Shen Y, Shen R, Ye Y (2018) Facile formation of nitrocellulose-coated Al/Bi$_2$O$_3$ nanothermites with excellent energy output and improved electrostatic discharge safety. Mater Design 143:93–103. https://doi.org/10.1016/j.matdes.2018.01.056

Damse RS, Omprakash B, Tope BG, Chakraborthy TK, Singh A (2009) Study of N-n-butyl-N-(2- nitroxyethyl) nitramine in RDX based gun propellant. J Hazard Mater 167:1222–1225. https://doi.org/10.1016/j.jhazmat.2008.12.095

Gao X, Jiang L, Xu Q (2019) Experimental and Theoretical Study on Thermal Kinetics and Reactive Mechanism of Nitrocellulose Pyrolysis by Traditional Multi Kinetics and Modeling Reconstruction. J Hazard Mater 386:121645. https://doi.org/10.1016/j.jhazmat.2019.121645

García-Garrido C, Pérez- Maqueda LA, Criado JM, Sánchez-Jiménez PE (2018) Combined kinetic analysis of multistep processes of thermal decomposition of polydimethylsiloxane silicone. Polymer 153:558–564. https://doi.org/10.1016/j.polymer.2018.08.045

Gratien A, Nilsson E, Doussin JF, Johnson MS, Nielsen CJ, Stenstrom Y, Picquet-Varrault B (2007) UV and IR absorption cross-sections of HCHO, HCDO, and DCDO. J Phys Chem A 111:11506–11513. https://doi.org/10.1021/jp074288r

Guo Y, Zhao N, Zhang T, Gong H, Ma H, An T, Zhao F, Hu R (2019) Compatibility and thermal decomposition mechanism of nitrocellulose/Cr$_2$O$_3$ nanoparticles studied using DSC and TG-FTIR. RSC Adv 9:3927–3937. https://doi.org/10.1039/c8ra09632e

Hadigheh SA, Wei Y, Kashi S (2021) Optimisation of CFRP composite recycling process based on energy consumption, kinetic behaviour and thermal degradation mechanism of recycled carbon fibre. J Clean Prod 292:125994. https://doi.org/10.1016/j.jclepro.2021.125994

Hao G, Zhou X, Liu X, Gou B, Hu Y, Xiao L, Liu J, Jiang W, Zhao F, Gao H (2019) Catalytic activity of nano-sized CuO on AP-CMDB propellant. J Energ Mater 37(4):484–495. https://doi.org/10.1080/07370652.2019.1657203

Hu Y, Tao B, Shang F, Zhou M, Hao D, Fan R, Xia D, Yang Y, Pang A, Lin K (2020) Thermal decomposition of ammonium perchlorate over perovskite catalysts: catalytic decomposition behavior, mechanism and application. Appl Surf Sci 513:145849. https://doi.org/10.1016/j.apsusc.2020.145849

Jain S, Park W, Chen YP, Qiao L (2016) Flame speed enhancement of a nitrocellulose monopropellant using graphene microstructures. J Appl Phys 120(17):174902. https://doi.org/10.1063/1.4966933

Katoh K, Higashi E, Nakano K, Ito S, Wada Y, Kasamatsu J, Miya H, Yamamoto M, Wada Y (2010) Thermal behavior of nitrocellulose with inorganic salts and their mechanistic action. Propell Explos Pyrot 35(5):461–467. https://doi.org/10.1002/prep.200900074

Kim JH, Cha JK, Cho MH, Kim H, Shim H-M, Kim SH (2019a) Thermal reactions of nitrocellulose- encapsulated Al/CuO nanoenergetic materials fabricated in the gas and liquid phases. Mater Chem Phys 238:121955. https://doi.org/10.1016/j.matchemphys.2019.121955

Kim M, Ko H, Park S-M (2019b) Synergistic effects of amine-modified ammonium polyphosphate on curing behaviors and flame retardation properties of epoxy composites. Compos B Eng 170:19–30. https://doi.org/10.1016/j.compositesb.2019.04.016

Krumlinde P, Ek S, Tunestål E, Hafstrand A (2016) Synthesis and characterization of novel stabilizers for nitrocellulose-based propellants. Propell Explos Pyrot 42(1):78–83. https://doi.org/10.1002/prep.201600122

Li Y, Chenxia K, Huang C, Cheng Y (2012) Effect of MnC$_2$O$_4$ nanoparticles on the thermal decomposition of TEGDN/NC propellant. J Therm Anal Calorim 109:171–176. https://doi.org/10.1007/s10973-011-1694-3

Li R, Xu H, Hu H, Yang G, Wang J, Shen J (2013) Microstructured Al/Fe$_2$O$_3$/nitrocellulose energetic fibers realized by electrospinning. J Energ Mater 32(1):50–59. https://doi.org/10.1080/07370652.2012.754515

Liang L, Guo X, Liang Z, Li G (2018) Preparation of PbCO$_3$–CuO nanoparticles and catalytic performance on NC/NG and NC/NG/NQ propellants. J Energ Mater 36(3):339–351. https://doi.org/10.1080/07370652.2018.1424969

Liu Q, Sun J, Han D, Liu X, Gao X, Jiang Y, Xie K (2020) Highly efficient photocatalytic removal of methylene blue by lamellar structured nanocrystalline and amorphous CuO. Mater Lett 276:128217. https://doi.org/10.1016/j.matlet.2020.128217

Mamleev V, Bourbigot S, Bras ML, Lefebvre J (2004) Three model-free methods for calculation of activation energy in TG. J Therm Anal Calorim 78(3):1009–1027. https://doi.org/10.1007/s10973-004-0467-7

Mei X, Zhong G, Cheng Y (2019) Ignition and combustion characteristics of aluminum/manganese iodate/nitrocellulose biocidal nanothermites. J Therm Anal Calorim

138:425–432. https://doi.org/10.1007/s10973-019-08226-4

Mendonça-Filho LG, Rodrigues RLB, Rosato R, Galante EBF, Nichele J (2019) Combined evaluation of nitrocellulose-based propellants: toxicity, performance, and erosivity. J Energ Mater 37(3):293–308. https://doi.org/10.1080/07370652.2019.1606867

Pang W, De Luca LT, Wang K, Fu X, Li J, Xu H, Fan X, Li H (2019) Chapter 7-Performance of composite solid propellant containing nanosized metal particles. Nanomaterials in Rocket Propulsion Systems, 263–298. https://doi.org/10.1016/b978-0-12-813908-0.00007-1

Pérez-Maqueda LA, Criado JM, Sánchez-Jiménez PE (2006) Combined kinetic analysis of solid-state reactions: a powerful tool for the simultaneous determination of kinetic parameters and the kinetic model without previous assumptions on the reaction mechanism. J Phys Chem A 110(45):12456–12462. https://doi.org/10.1021/jp064792g

Pourmortazavi SM, Hosseini SG, Rahimi-Nasrabadi M, Hajimirsadeghi SS, Momenian H (2009) Effect of nitrate content on thermal decomposition of nitrocellulose. J Hazard Mater 162(2–3):1141–1144. https://doi.org/10.1016/j.jhazmat.2008.05.161

Pourmortazavi SM, Sadri M, Rahimi-Nasrabadi M, Shamsipur M, Jabbarzade Y, Khalaki MS, Abdollahi M, Shariatinia Z, Kohsari I, Atifeh SM (2014) Thermal decomposition kinetics of electrospun azidodeoxy cellulose nitrate and polyurethane nanofibers. J Therm Anal Calorim 119(1):281–290. https://doi.org/10.1007/s10973-014-4064-0

Pourmortazavi SM, Kohsari I, Zandavar H, Koudehi MF, Mirsadeghi S (2019) Electrospinning and thermal characterization of nitrocellulose nanofibers containing a composite of diaminofurazan, aluminum nano-powder and iron oxide nanoparticles. Cellulose 26:4405–4415. https://doi.org/10.1007/s10570-019-02388-y

Ru C, Wang F, Xu J, Dai J, Shen Y, Ye Y, Zhu P, Shen R (2016) Superior performance of a MEMS-based solid propellant microthruster (SPM) array with nanothermites. Microsyst Technol 23(8):3161–3174. https://doi.org/10.1007/s00542-016-3159-x

Saceleanu F, Idir M, Chaumeix N, Wen JZ (2018) Combustion characteristics of physically mixed 40 nm aluminum/copper oxide nanothermites using laser ignition. Front Chem 6:465. https://doi.org/10.3389/fchem.2018.00465

Sánchez-Jiménez PE, Pérez-Maqueda LA, Perejón A, Criado JM (2010) Generalized kinetic master plots for the thermal degradation of polymers following a random scission mechanism. J Phys Chem A 114:7868–7876. https://doi.org/10.1021/jp103171h

Sánchez-Jiménez PE, Pérez-Maqueda LA, Perejón A, Criado JM (2013) Generalized master plots as a straightforward approach for determining the kinetic model: the case of cellulose pyrolysis. Thermochim Acta 552:54–59. https://doi.org/10.1016/j.tca.2012.11.003

Shehata AB, Hassan MA, Nour MA (2003) Effect of new poly 2-acryloyl-n, n'-bis (4-nitrophenyl) propandiamide and poly 2-acryloyl-n, n'-bis (4-methylphenyl) propandiamide and their synergistic action on the stability of nitrocellulose. J Hazard Mater 102(2–3):121–136. https://doi.org/10.1016/S0304-3894(03)00138-9

Shen J, Liu Z, Xu B, Liang H, Zhu Y, Liao X, Wang Z (2019) Inside cover: influence of carbon nanofibers on thermal and mechanical properties of NC-TEGDN-RDX triple-base gun propellants (Prop., Explos., Pyrotech. 3/2019). Propell Explos Pyrot 44(3):254–254. https://doi.org/10.1002/prep.201980302

Sing KSW, Everett DH, Haul RAW, Moscou L, Pierotti RA, Rouquerol J, Siemieniewska T (1985) Reporting physisorption data for gas/solid systems with special reference to the determination of surface area and porosity. Pure Appl Chem 57(4):603–619. https://doi.org/10.1351/pac198557040603

Singh G, Kapoor IPS, Dubey S (2009) Bimetallic nanoalloys: preparation, characterization and their catalytic activity. J Alloys Comp 480(2):270–274. https://doi.org/10.1016/j.jallcom.2009.02.024

Stiegman AE, Park C-D, Mileham M, van de Burgt LJ, Kramer MP (2009) Dynamics of Al/Fe$_2$O$_3$ MIC combustion from short single-pulse photothermal initiation and time-resolved spectroscopy. Propell Explos Pyrot 34(4):293–296. https://doi.org/10.1002/prep.200800021

Tarchoun AF, Trache D, Klapötke TM, Chelouche S, Derradji M, Bessa W, Mezroua A (2019) A promising energetic polymer from posidonia oceanica brown algae: synthesis, characterization, and kinetic modeling. Macromol Chem Phys. https://doi.org/10.1002/macp.201900358

Tarchoun AF, Trache D, Klapötke TM, Belmerabet M, Abdelaziz A, Derradji M, Belgacemi R (2020a) Synthesis, characterization, and thermal decomposition kinetics of nitrogen-rich energetic biopolymers from aminated giant reed cellulosic fibers. Ind Eng Chem Res 59(52):22677–22689. https://doi.org/10.1021/acs.iecr.0c05448

Tarchoun AF, Trache D, Klapötke TM, Khimeche K (2020b) Tetrazole-functionalized microcrystalline cellulose: a promising biopolymer for advanced energetic materials. Chem Eng J 400:125960. https://doi.org/10.1016/j.cej.2020.125960

Tarchoun AF, Trache D, Klapötke TM, Krumm B, Khimeche K, Mezroua A (2020c) A promising energetic biopolymer based on azide-functionalized microcrystalline cellulose: synthesis and characterization. Carbohyd Polym 249:116820. https://doi.org/10.1016/j.carbpol.2020.116820

Tarchoun AF, Trache D, Klapötke TM, Abdelaziz A, Derradji M, Bekhouche S (2021) Chemical design and characterization of cellulosic derivatives containing high-nitrogen functional groups: Towards the next generation of energetic biopolymers. Def Technol. https://doi.org/10.1016/j.dt.2021.03.009

Tarchoun AF, Trache D, Klapötke TM, Krumm B, Kofen M (2021b) Synthesis and characterization of new insensitive and high-energy dense cellulosic biopolymers. Fuel 292:120347. https://doi.org/10.1016/j.fuel.2021.120347

Tarchoun AF, Trache D, Klapötke TM, Selmani A, Saada M, Chelouche S, Mezroua A, Abdelaziz A (2021c) New insensitive high-energy dense biopolymers from giant reed cellulosic fibers: their synthesis, characterization, and non-isothermal decomposition kinetics. New J Chem 45:5099–5113. https://doi.org/10.1039/D0NJ05484D

Thomas JC, Sammet T, Dillier CA, Demko AR, Rodriguez, Petersen EL (2018) Effects of aging on the burning rates of composite solid propellants with and without nano-sized additives. 54th AIAA Joint Propulsion Conference. https://doi.org/10.2514/6.2018-4960

Thommes M, Kaneko K, Neimark Alexander V, Olivier James P, Rodriguez-Reinoso F, Rouquerol J, Sing Kenneth SW (2015) Physisorption of gases, with special reference to the evaluation of surface area and pore size distribution (IUPAC Technical Report). Pure Appl Chem 87(9–10):1051–1069. https://doi.org/10.1515/ci-2016-0119

Trache D, Tarchoun AF (2017) Stabilizers for nitrate ester-based energetic materials and their mechanism of action: a state-of-the-art review. J Mater Sci 53(1):100–123. https://doi.org/10.1007/s10853-017-1474-y

Wang Y, Song X, Song D, Liang L, An C, Wang J (2016) Synthesis, thermolysis, and sensitivities of HMX/NC energetic nanocomposites. J Hazard Mater 312:73–83. https://doi.org/10.1016/j.jhazmat.2016.03.043

Wei W, Jiang X, Lu L, Yang X, Wang X (2009) Study on the catalytic effect of NiO nanoparticles on the thermal decomposition of TEGDN/NC propellant. J Hazard Mater 168(2–3):838–842. https://doi.org/10.1016/j.jhazmat.2009.02.102

Wei WX, Cui BB, Jiang XH, Lu LD (2010) The catalytic effect of NiO on thermal decomposition of nitrocellulose. J Therm Anal Calorim 102(3):863–866. https://doi.org/10.1007/s10973-010-0695-y

Xu L, Jiang Y, Wang L (2017) Thermal decomposition of rape straw: pyrolysis modeling and kinetic study via particle swarm optimization. Energ Convers Manage 146:124–133. https://doi.org/10.1016/j.enconman.2017.05.020

Yan QL, Zhao FQ, Kuo KK, Zhang XH, Zeman S, DeLuca LT (2016) Catalytic effects of nano additives on decomposition and combustion of RDX-, HMX-, and AP-based energetic compositions. Prog Energ Combust 57:75–136. https://doi.org/10.1016/j.pecs.2016.08.002

Yang X, Wang Y, Li Y, Li Z, Song T, Liu X, Hao J (2017) Thermal stability and mechanical properties of hybrid materials based on nitrocellulose grafted by aminopropy-lisobutyl polyhedral oligomeric silsesquioxane. Polimery 62:576–587. https://doi.org/10.14314/polimery.2017.576

Yao E, Zhao N, Qin Z, Ma H, Li H, Xu S, An T, Yi J, Zhao F (2020) Thermal decomposition behavior and thermal safety of nitrocellulose with different shape CuO and Al/CuO nanothermites. Nanomaterials 10(4):725. https://doi.org/10.3390/nano10040725

Yoon J, Lee J, Choi B, Lee D, Kim DH, Kim DM, Moon D, Lim M, Kim S, Choi S-J (2016) Flammable carbon nanotube transistors on a nitrocellulose paper substrate for transient electronics. Nano Res 10(1):87–96. https://doi.org/10.1007/s12274-016-1268-6

Yu X, Zhang J, Zhang J, Niu J, Zhao J, Wei Y, Yao B (2019) Photocatalytic degradation of ciprofloxacin using Zn-doped Cu$_2$O particles: analysis of degradation pathways and intermediates. Chem Eng J 374:316–327. https://doi.org/10.1016/j.cej.2019.05.177

Zhao N, He C, Liu J, Gong H, An T, Xu H, Zhao F, Hu R, Ma H, Zhang J (2014) Dependence of catalytic properties of Al/Fe$_2$O$_3$ thermites on morphology of Fe$_2$O$_3$ particles in combustion reactions. J Solid State Chem 219:67–73. https://doi.org/10.1016/j.jssc.2014.06.039

Zhao N, Li J, Gong H, An T, Zhao F, Yang A, Hu R, Ma H (2016a) Effects of α-Fe$_2$O$_3$ nanoparticles on the thermal behavior and non-isothermal decomposition kinetics of nitrocellulose. J Anal Appl Pyrol 120:165–173. https://doi.org/10.1016/j.jaap.2016.05.002

Zhao N, Li J, Zhao F, An T, Hu R, Ma H (2016b) Combustion catalyst: nano-Fe$_2$O$_3$ and nano-thermite Al/Fe$_2$O$_3$ with different shapes. Dev Combust Technol. https://doi.org/10.5772/64748

Zhao N, Ma H, An T, Zhao F, Hu R (2016c) Effects of superthermite Al/Fe$_2$O$_3$ on the thermal decomposition characteristics of nitrocellulose. Chinese J Explos Propell 39(5):84–92

Zhongliang M, Le Q, Wei H, Liming H (2019) A novel approach on the study of cure kinetics for rheological isothermal and non-isothermal methods. Compos B Eng 162:242–249. https://doi.org/10.1016/j.compositesb.2018.10.066